SCIENTIFIC REPORTS

OPEN

SUBJECT AREAS:
FERROELECTRICS AND MULTIFERROICS
CONDENSED MATTER PHYSICS

Received
26 March 2014

Accepted
1 May 2014

Published
21 May 2014

Correspondence and requests for materials should be addressed to J.-M.L. (liujm@nju.edu.cn)

Kinetics of 90° domain wall motions and high frequency mesoscopic dielectric response in strained ferroelectrics: A phase-field simulation

P. Chu[1], D. P. Chen[1], Y. L. Wang[1], Y. L. Xie[1], Z. B. Yan[1], J. G. Wan[1], J.-M. Liu[1] & J. Y. Li[2]

[1]Laboratory of Solid State Microstructures, Nanjing University, Nanjing 210093, China, [2]Department of Mechanical Engineering, University of Washington, Seattle, WA 98195, USA.

The dielectric and ferroelectric behaviors of a ferroelectric are substantially determined by its domain structure and domain wall dynamics at mesoscopic level. A relationship between the domain walls and high frequency mesoscopic dielectric response is highly appreciated for high frequency applications of ferroelectrics. In this work we investigate the low electric field driven motion of 90°-domain walls and the frequency-domain spectrum of dielectric permittivity in normally strained ferroelectric lattice using the phase-field simulations. It is revealed that, the high-frequency dielectric permittivity is spatially inhomogeneous and reaches the highest value on the 90°-domain walls. A tensile strain favors the parallel domains but suppresses the kinetics of the 90° domain wall motion driven by electric field, while the compressive strain results in the opposite behaviors. The physics underlying the wall motions and thus the dielectric response is associated with the long-range elastic energy. The major contribution to the dielectric response is from the polarization fluctuations on the 90°-domain walls, which are more mobile than those inside the domains. The relevance of the simulated results wth recent experiments is discussed.

Substantial efforts have been devoted to ferroelectric (FE) materials and their applications in advanced electronic technologies[1,2]. The core ingredients in the physics of ferroelectrics include electric polarization P and its static/dynamic responses to electric field E_{ext} or/and other stimuli. In the mesoscopic level, the dielectric and polarization responses of a ferroelectric are determined by the specific domain structure and realized by the domain wall motions. In particular, the high-frequency applications of ferroelectrics have received continuous attention. A number of FE materials in thin film form have been used for high-frequency devices in microwave and optical communications as well as computing applications because of their high dielectric permittivity[3,4]. A full understanding of the domain wall motion driven by either static or high-frequency dynamic force has been the core issue of the physics of ferroelectrics and the basis for their applications.

The FE domain wall motion is a complicated process and depends on a series of intrinsic particulars such as defects, domain structures, and strains[5–7]. The consequence of strain, a topic to be dealt with in this work, has been highly concerned. Besides conventional scope of ferroelasticity, an externally imposed strain in a paraelectric surprisingly enables remarkable ferroelectricity[8]. Externally imposed strain can modulate the FE phase transitions too[9–11]. These strain effects raise particular attention to FE thin films deposited on rigid substrates, in which the induced strain can be controlled due to the lattice mismatch of the substrates with the films. It thus allows the performance improvement of the FE thin films by means of 'strain-engineering' the FE domains in the mesoscopic level.

Along this line, the most interested issue is the strain effect in perovskite FE oxide thin films with tetragonal lattice symmetry like $BaTiO_3$ and $PbTiO_3$. First, epitaxial $BaTiO_3$ and $PbTiO_3$ thin films deposited on substrates such as $SrTiO_3$, $LaAlO_3$, and MgO, are often explored not only for fundamental understanding but also for potential applications, while textured polycrystalline films are also investigated. Second, these thin films offer regular twin-like (stripe-like) 90°-domain structure in coexistence with 180°-domains due to the intrinsic ferroelastic effects. In most cases, the 90° ferroelastic domains are dominant, and the order parameter is strongly coupled to the strains. Furthermore, the substrate induced strain imposes a competitive or coherent coupling with the internal ferroelastic strain in the films, making the domain structure and domain wall motion complicated.

These behaviors, particularly in the high frequency range, are much less studied. It is believed that externally imposed strains have strong impacts on the domain wall motion and thus the high frequency dielectric permittivity[12–14].

A prominent feature of the strain effects is the 90° domain walls vibration in response to an *ac* electric field of high frequency, while the static responses have been well addressed. The dynamics of the domain wall may be characterized by the variation in dielectric permittivity as a function of the *ac* electric field (frequency ω and amplitude E_0), as long as the domain structure is well defined. A recent experiment demonstrating this dielectric response was carried out on clamped $Pb(Zr_{1-x}Ti_x)O_3$ (PZT) thin films deposited on Si substrates[15]. By creating cavities beneath the Pt/PZT/Si capacitors and cracking, these released PZT films show dramatic variation in the global dielectric nonlinearity and the frequency dependence as a function of mechanical clamping. The sequent piezoelectric examinations show that the increased local mobility of domain walls must be responsible for these behaviors, where "mobility" refers to the capability of domain walls in response to stimuli. This work among many others raises an important issue on how the 90°-domain structures in FE thin films couple dynamically with externally imposed strains[16]. This question motivates us to investigate the dynamics of domain walls in the 90° domain structure modulated by strains, and consequently the dielectric responses at the mesoccopic level.

While the strain coupling in polycrystalline PZT thin films may be too complicated, our purpose is to focus on tetragonal FE lattice (e.g. $BaTiO_3$ or $PbTiO_3$) and reveal the dynamics of the 90°-domain structure which couples the internal ferroelastic strains with externally imposed normal strains, in response to electric field E_{ext}. Instead of addressing the dynamic motion equation[17–19], we perform the phase-field simulations by which a continuous distribution function of the domain orientations is used to characterize the domain wall motion[20,21]. Such a phenomenological method enables us to directly examine the mesoscopic picture of these dynamic processes. We also investigate the underlying mechanism with which the strains modulate the domain wall motion in the energy landscape. In this phase-field model, the dipole-dipole and elastic interactions are considered[22], since these long-range interactions play an important role in configuring the domain structure[17,23]. The strain vector appears as an order parameter and can be modulated by external load.

We consider a tetragonal FE system as approached by an $L \times L$ two-dimensional (2D) lattice with periodic boundary conditions[24], and start from the Ginzburg-Landau theory. On each site, an electric dipole $P(r)=(P_x, P_y)$ normalized by a pre-factor P_a[25] and an elastic displacement vector $u(r)=(u_x, u_y)$ are imposed. We clarify that our simulation is not necessarily associated with a thin film, although the electric dipoles in our simulation can only relax on the in-plane configuration. An extension of the results to other geometry is plausible. For simplification, our simulation will not deal with the finite boundary problem since it will introduce complicated corrections to the mechanical balance[25], while open-circuit boundary issue will only be discussed briefly. Given this assumption, the lattice can be mapped into a small region of real material. By these approximations, we can focus on the details of the local dielectric response in mesoscopic scale.

The electric field $E_{ext}=(E_x, E_y)$ is confined on the lattice plane. The total free energy for this FE lattice can be written as[26]:

$$F = F_{ld} + F_g + F_{dd} + F_{el} + F_{es} + F_{se}, \tag{1}$$

where F_{ld}, F_g, F_{dd}, F_{el}, F_{es}, and F_{se} are the Landau potential, gradient energy, dipole-dipole interaction, elastic energy, electrostrictive energy, and electrostatic energy, respectively. Term F_{ld} extending to the sixth-order is written as:

$$\begin{aligned} F_{ld} = \sum_{\langle i \rangle} & A_1\left(P_x^2+P_y^2\right) + A_{11}\left(P_x^4+P_y^4\right) + A_{12}P_x^2P_y^2, \\ & + A_{111}\left(P_x^6+P_y^6\right) + A_{112}\left(P_x^2P_y^4+P_x^4P_y^2\right) \end{aligned} \tag{2}$$

where A_1, A_{11}, A_{12}, A_{111} and A_{112} are the Landau expansion coefficients and $A_1=A_{10}(T-T_0)$. The lowest-order expression of term F_g is:

$$\begin{aligned} F_g = \sum_{<i>} \frac{1}{2} \Big[& G_{11}\left(P_{x,x}^2+P_{y,y}^2\right) + G_{12}P_{x,x}P_{y,y} \\ & + G_{44}\left(P_{x,y}+P_{y,x}\right)^2 + G'_{44}\left(P_{x,y}-P_{y,x}\right)^2 \Big], \end{aligned} \tag{3}$$

where $P_{i,j}=\partial P_i/\partial r_j$ and $r_j=(x, y)$, and G_{11}, G_{12}, G_{44} and G'_{44} are the gradient energy coefficients[20]. Terms F_{dd} and F_{se} can be written respectively as:

$$F_{dd} = -\frac{1}{4\pi\varepsilon} \sum_{<i>} \sum_{<j>} \frac{P(r_i)\cdot P(r_j)}{|r_i-r_j|^3} - \frac{3P(r_i)\cdot(r_i-r_j)\left[P(r_j)\cdot(r_i-r_j)\right]}{|r_i-r_j|^5}, \tag{4}$$

$$F_{se} = -E_{ext}\cdot \sum_{<i>} P_i,\ E_{ext}=(E_x,E_y), \tag{5}$$

where F_{dd} includes two contributions. One is the anisotropic part $F_{dep}(P_0)$ and the other is the isotropic part $F'_{dd}(\delta P)$ if we treat $P(r)=P_0+\delta P(r)$ where P_0 is the spatially homogeneous average polarization and r is the spatial vector. It is noted that P_0 can be defined by:

$$\int_V \delta P(r) dV = \int_V \delta P(r) dr^3 = 0, \tag{6}$$

where V is the volume of lattice.

Term $F_{dep}(P_0)$ describes the depolarization energy and shares the same form as F_{se} by difference of a 1/2 factor. In real system, the depolarization field is compensated by free charges for the cases with open boundaries. For the present case, no free charge is included. The effective electric field is independent of the depolarization field and simply equivalent to E_{ext}. In experiments, the electric field is usually applied via the electrodes in close-circuit which introduces free charge onto the interface. This will cancel out the depolarization field. Term F_{dd} counts an integration over the whole lattice, and a realistic calculation is done either by the Fourier transformation or by finite truncation treatment[27,28]. For a 2D lattice, the finite truncation is a sufficiently accurate approximation as long as the truncating distance R is big ($R=8$ in our simulation)[24,29,30].

The elastic energy F_{el} yields:

$$\begin{aligned} F_{el} = & \sum_{<i>} \frac{1}{2} C_{11}\left(u_{x,x}^2+u_{y,y}^2\right) + C_{12}u_{x,x}u_{y,y} + \frac{1}{2}C_{44}u_{x,y}^2, \\ & u_{i,i}=\partial u_i/\partial r_i,\ u_{i,j}=\partial u_i/\partial r_j + \partial u_j/\partial r_i \text{ if } i\neq j \end{aligned} \tag{7}$$

where C_{ij} is the elastic stiffness tensor which has only three independent elastic constants for a square lattice.

The electrostrictive energy F_{es} is:

$$F_{es} = -\sum_{<i>} u_{x,x}(q_{11}P_x^2+q_{12}P_y^2) + u_{y,y}(q_{11}P_y^2+q_{12}P_x^2) + u_{x,y}q_{44}P_xP_y, \tag{8}$$

where $q_{11}=C_{11}Q_{11}+2C_{12}Q_{12}$, $q_{12}=C_{11}Q_{12}+2C_{12}(Q_{11}+Q_{12})$, and $q_{44}=2C_{44}Q_{44}$ are the effective electrostrictive coefficients, Q_{ij} are the electrostrictive coefficients in external stress free state. Mathematically, we can also separate the total strain η_{ij} into a homogenous component η_0, and a heterogeneous one $\delta\eta_{ij}$ which denotes the microscopic strain distribution at site (i, j)[22,25]:

$$\eta_{ij}(r) = \eta_0 + \delta\eta_{ij}(r). \tag{9}$$

here external strain η_0 is imposed either by a substrate or an external load. Similar to generally accepted treatment[20,22,28], order parameter $u(r)$ is reduced to a function of $P(r)$[31]. The step-by-step procedure of this derivation can be found in the Supplementary materials. To access the dielectric response over frequency domain, we compute dielectric permittivity $\varepsilon(\omega)$ over a broad range of frequency. The algorithms are presented in the Method section. The parameters for the simulations are listed in Table I, and for the details of the simulation procedure one can refer to earlier works[32,33].

Results

Domain wall kinetics under dc electric field. We first investigate the 90°-domain wall motion driven by a static (*dc*) E_{ext}. To characterize the wall motion, we define the domain width l deviating from the equilibrium width l_0 under zero electric field. Thus, $\Delta l = l - l_0$ stands for the offset in response to E_{ext}. In order to minimize the effect of domain wall irregularity, parameters l and l_0 are calculated indirectly. A set of rectangle-like regions, whose two sides are on the domain walls to enable their areas as big as possible, are taken. We sum the areas of these rectangles. The local domain width l is obtained by dividing the area by its length and then performing statistics over sufficient number of rectangles in the same region.

In Figure 1 is shown the kinetics of field-driven domain wall motion, given different strains from slightly compressive ones to tensile ones. Both E_{ext} and η_0 are along the y-axis, thus the l indicates the width of a_2-domain where the dipoles align along the y-axis. The evaluated $\Delta l(t)$ data are plotted in Figure 1(a) where the applied strains are labeled numerically. For each strain, $\Delta l(t)$ shows similar behavior and increases rapidly in the early stage and tends to be saturated at Δl_{max} in the late stage. Nevertheless, Δl_{max} depends on η_0, and the bigger η_0 the smaller Δl_{max}. In Figure 1(b) we plot the evaluated $l_0(\eta_0)$ for the a_2-domain and corresponding $\Delta l_{max}(\eta_0)$, showing the monotonous increasing of $l_0(\eta_0)$ and decreasing of $\Delta l_{max}(\eta_0)$. For definition of each symbol and motion pattern of domain wall, one can refer to the Supplement materials.

The kinetics of wall motion was investigated earlier[34] and can be described by a simple model[17,23], yielding the kinetic equation $\Delta l(t) = a(1\text{-}e^{-bt})$ where $a = \Delta l_{max}$ and b are the fitting parameters. As shown in Figure 1(c), the monotonous decrease and increase of a and b as a function of η_0 respectively imply that the a_2-domain extension becomes tougher upon the transition from compressive strain to tensile one. It is also possible to evaluate the initial motion speed of the a_2-domain walls by taking $v_0 = d\Delta l/dt|_{t\to 0} = ab$, as shown in Figure 1(d), consistent with the above argument. In other words, for compressive strain ($\eta_0 < 0$), the motion speed of domain walls is higher than that for tensile strain ($\eta_0 > 0$).

For the cases with strain η_0 not parallel to E_{ext}, the above analysis is qualitatively correct. The tensile strain makes the domains with $P//\eta_0$ wider and the compressive one makes it narrower. This behavior allows a competition between the strain effect and electric field effect, and they can be coherent or cancelled depending on their orientation relationship. However, when the strain contains shear components, the situation becomes more complicated and extensive calculation is not discussed here.

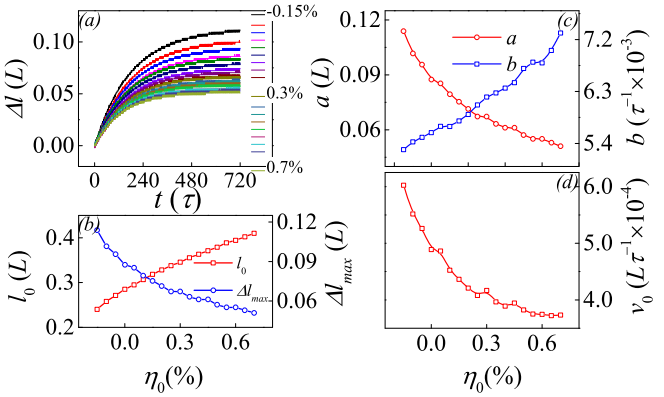

Figure 1 | Evaluated parameter Δl as a function of time t given a series of η_0 labeled numerically (a), l_0 and Δl_{max} as a function of η_0 respectively (b), parameters a and b as a function of η_0 respectively (c), and initial domain wall motion speed v_0 as a function of η_0 (d). $E_{ext} = 6|A_1|P_a$.

Domain wall vibrations and dielectric response: $\eta_0 = 0$. Based on the above result, one understands that the 90°-domain structure clamped by external stress has different stability characteristics from the stress-free state. This difference can be discussed in the clamped 90°-domain structure driven by the *ac*-electric field, characterized by variation of dielectric permittivity as a function of η_0. In particular, the dielectric response in the frequency domain is related to the wall motion.

We first address the dielectric response in $\eta_0 = 0$. Figure 2(a) and (b) show the real part $\varepsilon_r(f)$ and imaginary part $\varepsilon_i(f)$ at three θ angles. Here a small $E_0 = 0.6|A_1|P_a$ is chosen, with the field direction defined by angle θ between the x-axis and E_{ext}. In general, $\varepsilon_r(f)$ decreases gradually with increasing f for all the three cases, while $\varepsilon_i(f)$ shows two peaks at characteristic frequencies $f_L \sim 0.1\tau^{-1}$ and $f_H \sim 7\tau^{-1}$, which are respectively referred as the low-f and high-f dispersions. Here $\tau = 1/|A_1|D$ is the characteristic time for electric dipole flip (see the Method section for details). The striking feature is the low-f dispersion anisotropy, i.e. the θ-dependence which is the most remarkable at $\theta = 90°$ (and $\theta = 0$ too, four-fold symmetry). This θ-dependence is shown by $\varepsilon_r(\theta)$ at $f = 0.01\tau^{-1}$ as an example in Figure 2(c), characterized by the typical periodic variation.

The above behaviors can be understood by investigating the instant evolution of domain structure. By turning E_{ext} from $\theta = 0$ to $\theta = 180°$, one checks the domain evolution and dielectric dispersion. The low-f dispersion is related to the domain wall vibrations, while the high-f dispersion is attributed to the flip of individual dipoles. In fact, the dispersion peak around f_H is also observed in the mono-domain lattice.

Now we investigate the origin for the low-f dispersion anisotropy in the domain scale. In $\eta_0 = 0$, the spatial distributions of ε_r at $f = 0.05\tau^{-1}$ in four θ angles are presented in Figure 3(a)~(d), respectively, where the color scales the intensity ($\varepsilon_r = 0.0 \sim 1.0$). It is immediately seen that the dielectric permittivity mainly comes from the contribution of wall vibrations, while those dipoles deeply inside the

Table I | Physical parameters chosen for the simulation ($\tau^{-1} = |A_1|D$) [24, 25]. All these parameters appear in the dimensionless form

Parameter (unit)	Value	Parameter (unit)	Value	Parameter (unit)	Value
l	64~256	A_1^* ($\|A_1\|$)	−1.00	A_{11}^* ($A_{11}P_0^2/\|A_1\|$)	−0.24
A_{12}^* ($A_{12}P_0^2/\|A_1\|$)	2.50	A_{111}^* ($A_{111}P_0^4/\|A_1\|$)	0.49	A_{112}^* ($A_{112}P_0^4/\|A_1\|$)	1.20
G_{11}^* ($G_{11}/A_1^2\|A_1\|$)	1.60	G_{12}^* ($G_{12}/A_1^2\|A_1\|$)	0.00	G_{44}^* ($G_{44}/A_1^2\|A_1\|$)	0.80
G'^*_{44} ($G'_{44}/A_1^2\|A_1\|$)	0.80	C_{11}^* ($C_{11}/\|A_1\|P_0^2$)	2.75	C_{12}^* ($C_{12}/\|A_1\|P_0^2$)	1.79
C_{44}^* ($C_{44}/\|A_1\|P_0^2$)	0.543	q_{11}^* ($q_{11}/\|A_1\|$)	0.143	q_{12}^* ($q_{12}/\|A_1\|$)	−0.0074
q_{44}^* ($q_{44}/\|A_1\|$)	0.0157	τ^* (τ)	0.0004		

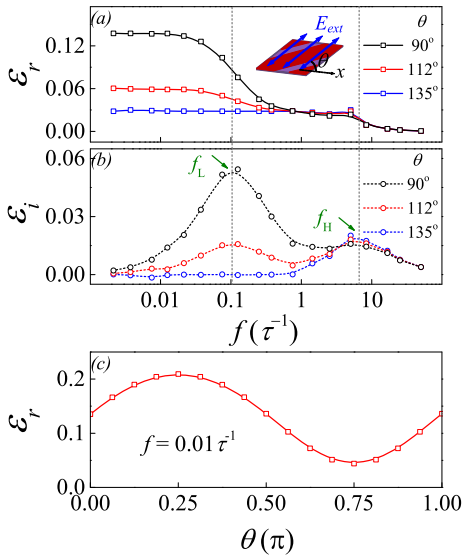

Figure 2 | Simulated dielectric permittivity spectra: (a) real part and (b) imaginary part over a wide range of frequency, at θ=90°, 112°, and 135°, respectively. (c) Dielectric permittivity real part ε_r as a function of angle θ at a constant f=0.01τ^{-1}.

domains contribute little. This characteristic makes the dielectric response very specific.

At θ=45°, the domain structure and dielectric response are shown in Figure 3(a). Again, the dielectric response mainly comes from the contribution of electric dipoles on the walls and near regions. This feature can be understood from the electrostatic energy -P·E_{ext}. The walls have the highest local mobility. No matter E_{ext} is positive or negative, there is always one of the neighboring two domains, inside which all the dipoles take the 135° angle from E_{ext}. This domain will shrink while the other will expand, making the wall move easily. This is also the reason why ε_r is the highest at θ=45°, as seen in Figure 2(c).

At θ=90° (or θ=0), as shown in Figure 3(b), the wall mobility is slightly lower, and ε_r is lower too. In this case, E_{ext} is parallel to the dipoles in one domain and perpendicular to those in the other. At θ=112° and θ=135°, as shown in Figure 3(c) and (d), respectively, the wall mobility falls down even further, resulting in even lower ε_r. The wall mobility becomes the lowest at θ=135°. Figure 3(d) shows

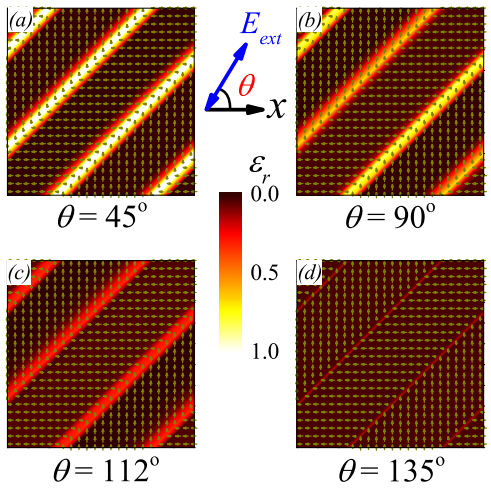

Figure 3 | **Snapshoted patterns of dielectric permittivity real part ε_r at constant frequency f=0.05τ^{-1} with angle θ=45° (a), 90° (b), 112° (c), and 135° (d).**

that almost the whole lattice has the identical ε_r except the very thin and dim lines on the walls. The reason is that term -P·E_{ext} in two neighboring domains are almost equivalent and they compete with each other, hindering the wall motion. The dielectric response is weak with no frequency dispersion.

We finally check the dielectric response in the high-f range and one example is given in Figure 4(a) and (b) at f=6τ^{-1} for two specific θ angles: θ=90° and θ=135°. The dielectric distribution over the whole lattice is roughly homogeneous. For details, one looks at the case in Figure 4(a) and finds only weak color contrast between the two neighboring domains a_1 and a_2. The domain a_1 whose dipoles align along the x-axis but perpendicular to E_{ext} shows slightly higher ε_r than that of domain a_2. The reason is obvious that the dipoles in domain a_1 are more fluctuating than those in domain a_2.

Domain wall vibrations and dielectric response: η_0>0. Now we discuss the cases with η_0≠0. We only present in details the results on normally strained lattice. When the lattice is normally strained, the domain structure is deformed. To clarify the similarity and difference between the strain-free and strained lattices, we consider the simplest situation: η_0=0.7% under E_{ext} with f=0.05τ^{-1} and E_0=0.6|A$_1$|P_a, both aligned along the y-axis (θ=90°). We present in Figure 4(c) and (d) the strain-free domain structure and strained structure respectively, as well as the spatial distribution of ε_r. For the two cases, the distributions are similar in amplitude but the high-ε_r spatial profiles across the domain walls are much wider for the strain-free lattice than those for the strained lattice. In the qualitative sense, the dielectric permittivity averaged over the whole strained lattice is lower than that over the strain-free lattice, at least in the low-f range. This η_0-dependence can be further illustrated in Figure 5(a), where $\varepsilon_r(f)$ and $\varepsilon_i(f)$ at three tensile strains (η_0=0, 0.2%, 0.7%) are plotted. Both the real and imaginary parts are remarkably suppressed by tensile strain, and the f_L has a slight shift towards the high-f side. We also calculate the instant responses of the Δl and polarization component P_y against E_{ext} at the three tensile strains, shown in Figure 5(b). The one-to-one correspondence between Δl, P_y, and E_{ext}, respectively, is observed. The responses of Δl and P_y are synchronous with E_{ext} in the low-f range, and delayed in the high-f range. Furthermore, the wall vibration amplitude is suppressed by the tensile strain.

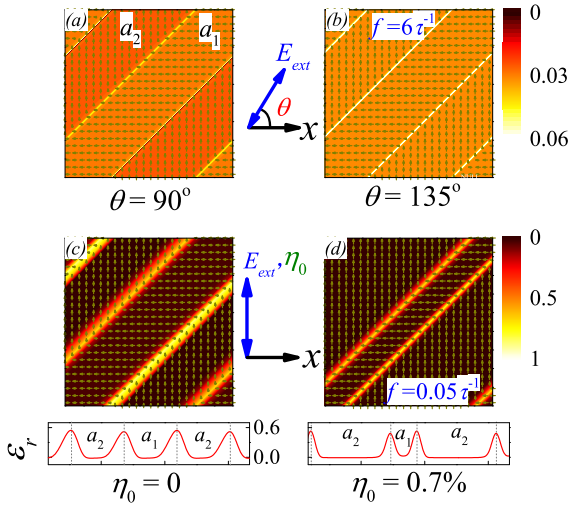

Figure 4 | Snapshoted patterns of dielectric permittivity real part ε_r at constant frequency f=6τ^{-1} with angle θ=90° (a) and 135° (b). At constant frequency f=0.05τ^{-1} with different tensile strains along the y-axis: (c) η_0=0 and (d) η_0=0.7%. The red lines below the snapshots indicate the alignment of ε_r along the [$\bar{1}$,1]. Hereafter, E_0=0.6|A$_1$|P_a.

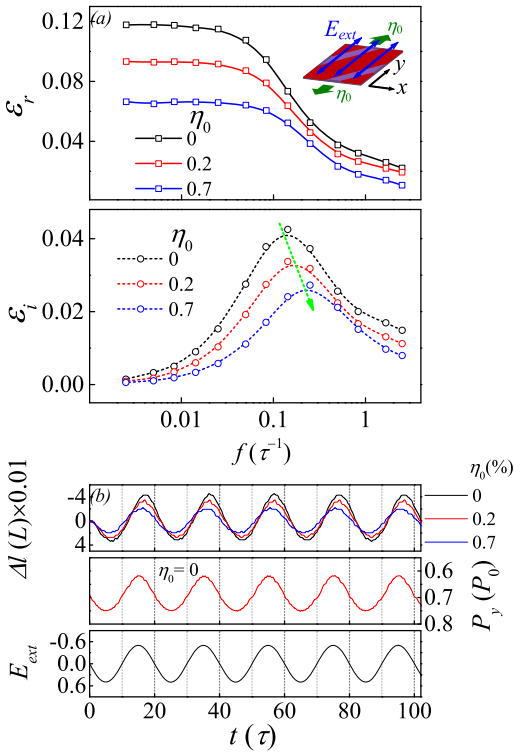

Figure 5 | (a) Simulated dielectric permittivity spectrum around $f=0.05\tau^{-1}$ given $\eta_0=0$, 0.2%, and 0.7% along the *y*-axis. (b) From top to bottom: parameter Δl as a function of time *t* given $\eta_0=0$, 0.2%, and 0.7% at $f=0.05\tau^{-1}$, the *y* component of total polarization as a function of time *t*, and the *ac* electric field E_{ext} as a function of time *t*. The *ac* electric filed is along *y*-axis, $E_0=0.6|A_1|P_a$.

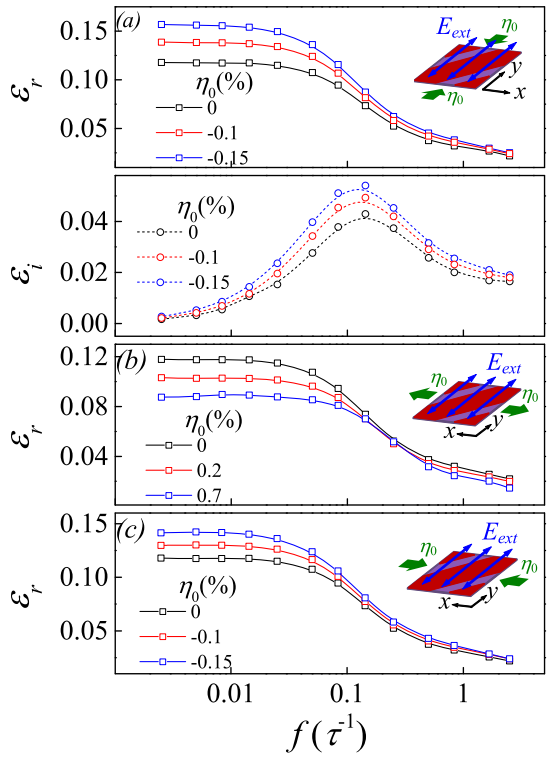

Figure 6 | (a) Simulated dielectric permittivity spectrum around $f=0.05\tau^{-1}$ given $\eta_0=0$, −0.1%, and −0.15% along the *y*-axis with the *ac* electric along the *y*-axis too. The calculated real part ε_r at tensile strain (b) and compressive strain (c) perpendicular to the *ac* electric field along the *y*-axis. $E_0=0.6|A_1|P_a$.

The above results refer to the simplest situation. When η_0 and E_{ext} are aligned along arbitrary directions independently, more complexity is seen in terms of the domain structure evolution and dielectric response. For some specific geometry, the strain and electric field may compete with each other. Some more discussion will be given below. However, in general, the calculated results are qualitatively similar to those for the simplest situation: the tensile strain suppresses the domain wall vibration, thus reducing the dielectric permittivity.

Domain wall vibrations and dielectric response: $\eta_0<0$. Now we check the cases with $\eta_0<0$. Referring to the results under static (*dc*) E_{ext}, as shown in Figure 1, one sees that the static compressive strain assists the 90° domain wall motion. It is thus expected that the dielectric permittivity in compressed lattice will increase. The η_0-dependences of $\varepsilon_r(f)$ in three compressive strains ($\eta_0=0$, −0.1%, −0.15%) along the *y*-axis are plotted in Figure 6(a), consistent with the expected results. Similar behaviors are observed for the strain and electric field both applied along the *x*-axis.

We also check the situations where E_{ext} is not parallel to η_0. One example is shown in Figure 6(b) for $\eta_0>0$ and Figure 6(c) for $\eta_0<0$, where E_{ext} is along the *y*-axis and η_0 is along the *x*-axis. Our extensive calculations establish the qualitatively similar behaviors: the tensile strain suppresses the 90° domain wall motion and thus the dielectric permittivity, while the compressive strain enhances the domain wall motion and the dielectric permittivity, no matter whether E_{ext} is not parallel to η_0 or not. We summarize spectrum $\varepsilon_r(f, \eta_0)$ in Figure 7(a) and (b). At $f<f_L$, such as $f=0.01\tau^{-1}$ and $0.05\tau^{-1}$, ε_r falls gradually with increasing η_0 from $\eta_0<0$ to $\eta_0>0$, while this tendency becomes negligible as $f>f_L$ such as $f=0.5\tau^{-1}$ since the single dipole response becomes dominant at this frequency. The overall evolution of $\varepsilon_r(f, \eta_0)$ is plotted in Figure 7(b).

Discussion

It should be mentioned that the periodic boundary conditions allows the total strains in all directions to be exactly balanced out, and the strain effect is of long-range and coupled with mechanical boundary conditions. However, if other mechanical boundary conditions are considered, such as free boundary, the total strains can be partially relaxed through the free boundaries. The 90°-domain walls can be more moveable and thus show more significant response to electric field, as partially discussed in Ref. 15.

To understand the simulated results, one may give additional discussion by looking at the energy landscape and comparing the simulated results and experiments, although relevant experimental data are really rare.

Energy landscape. We calculate the elastic energy distribution associated with the 90° domain structures. For a single domain lattice, the total strain field is homogeneous, thus accommodating extremely large elastic energy. The single domain is decomposed into the 90° domain structure so that the total elastic energy can be relaxed. Owing to the lattice volume conservation, for one domain, the compressive strain along one direction (e.g. the *x*-axis) is always accompanied with the tensile strain along the other direction (the *y*-axis), and verse vice. One can refer to the Supplement materials for the strain distribution.

First, we consider the $\eta_0=0$ case. Given a static electric field along the *y*-axis, the domain walls move into the a_1-domain in compensation with the extension of the a_2-domain width. The continuous shrinking of the a_1-domain is accompanied with the increasing magnitude of elastic strain (e_{xx} and e_{yy}) inside the a_1-domain. Since the total elastic energy is proportional to η^2, the rapidly enhanced total elastic energy inside the shrunk a_1-domain acts as the resistant force against the electric field, responsible for eventual termination of the

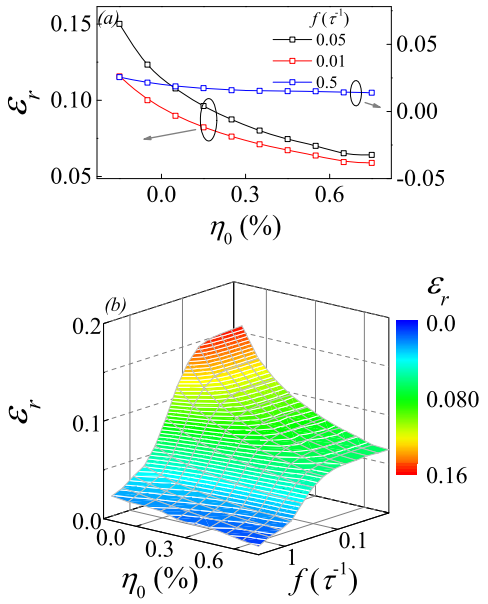

Figure 7 | (a) Simulated dielectric permittivity real part ε_r as a function of η_0 with the *ac* electric field frequency $f=0.01\tau^{-1}$, $0.05\tau^{-1}$, and $0.5\tau^{-1}$. (b) A 2D plot of ε_r as a function of η_0 and f. The *ac* electric field and strains are all along the y-axis. $E_0=0.6|A_1|P_a$.

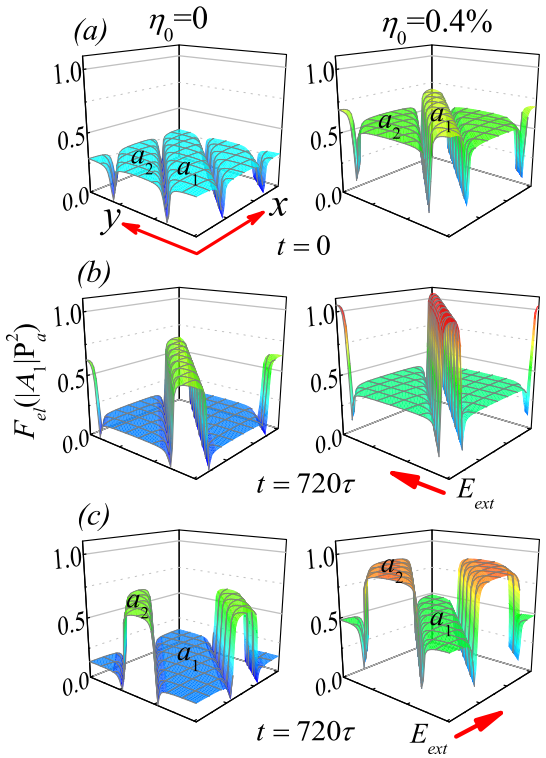

Figure 8 | **Evaluated spatial contours of elastic energy F_{el} in the 90°-domained lattice.** The left column (a) refers to $\eta_0=0$ and the right one (b) refers to $\eta_0=0.4\%$. The top row refers to $E_{ext}=0$, the middle row refers to $t=720\tau$ after E_{ext} (*dc*) along the y-axis applies to the lattice, and the bottom row refers to $t=720\tau$ given E_{ext} (*dc*) along the x-axis. $E_{ext}=6|A_1|P_a$.

wall motion when the a_1-domain becomes sufficiently narrow, as shown in the left column of Figure 8(a) and Figure 8(b), where the total elastic energy $F_{el}(x, y)$ is plotted. This explains why Δl tends to be saturated at Δl_{max} as time goes infinitive.

This scenario applies to the lattice with externally imposed strain. Take $\eta_0=0.4\%$ along the y-axis as an example. At $t=0$ with $E_{ext}=0$, the whole elastic energy distribution on the right column of Figure 8 shifts upward with respect to the case of $\eta_0=0$. However, one can observe a much higher energy distribution in the shrinking a_1-domains. Therefore, the a_1-domains are already under highly tensile state along the x-axis even at $E_{ext}=0$, when an externally imposed strain along the y-axis is applied. In this case, a static electric field along the y-axis may further force the wall moving into the a_1-domain but will be highly resisted by the high strain energy, as shown in the right column of Figure 8. Therefore, additional shrinking of the a_1-domain driven by the electric field would become even tougher, given that $\eta_0=0.4\%$ already makes the a_1-domain narrow.

If strain η_0 is applied along other orientations, no matter whether it is parallel to E_{ext} or not, the wall motion behaviors remain qualitatively similar. One example is given by applying E_{ext} along the x-axis where E_{ext} and η_0 are normal to each other. As shown in Figure 8(c), a strain η_0 along the y-axis enhances remarkably the total elastic energy in the a_2-domain, making the further shrinking of the a_2-domain more difficult than the case with $\eta_0=0$. Therefore, the above-discussed results don't lose the generality.

Comparison with experiments. The implication of the above simulation data can be checked by comparing the simulated results with experimental data on the contribution of domain wall vibrations to the dielectric response in $BaTiO_3$ (BTO) and $Pb(Zr_{1-x}Ti_x)O_3$ (PZT) ceramics[35–37], although these data have not yet received confirm from the direct detecting of the mesoscopic scale dielectric distribution across the 90° domain walls. Therefore, such comparisons may not be so direct in quantitative sense. For PZT, experiments[35] showed that above 10^{11} Hz the real part of dielectric constant begins to drop, due to the frozen dipole oscillators themselves. In our simulation, the corresponding frequency is assigned as $f_H = 7\tau^{-1}$ in Figure 2(a). Thus we have the characteristic inverse time scale $\tau^{-1} \sim 10^{10}$ s^{-1}, and the calculated $f_L \sim 10^9$ Hz.

Regarding the PZT ceramics, experimental data[36] also indicate the dielectric dispersion around 1.0 GHz, which was argued to arise from the vibrations of the frozen 90° domain walls. For the dielectric permittivity magnitude, we take the dimensionless factor $(|A_1|\varepsilon^*)^{-1} \sim 10^3$, where A_1 is 3.8(T-479) × 10^5C^{-2}m^{2}N taken from PZT and ε^* is the vacuum permittivity. The calculated real part of the dielectric permittivity at $\theta=45°$ is ~200, as shown in Figure 2(c), and the maximum of the imaginary part is ~100. Indeed, experimental measurements[37] on ceramics PZT (x=0.48–0.52) gave the difference in the real part between the extremely high frequency and the very low frequency, which is 250–500. The peak of the imaginary part is 150–265. These values agree roughly with our simulation results here. The above comparisons allow us to claim that the present calculations are reliable even in quantitative sense.

We also find some experimental results about the effects of tensile and compressive strains on the overall dielectric constant. In microwave frequency range, it was shown that dielectric constant and tunability of BTO films grown on MgO gradually decrease as the in-plane strain goes from the compressive type to tensile type[38]. Similar behaviors were observed in polycrystalline $Ba_{0.6}Sr_{0.4}TiO_3$ thin films upon increasing tensile strain[39]. Those results are consistent with our calculation in a qualitative sense. Unfortunately, none of those experiments establishes a clear logic between the dielectric response and the 90° domain wall motion, although the frequency range is properly related to the 90° domain wall vibration. Establishing this logic is a technical challenge for experimentalists. To reveal the domain wall response to external electric field, one may map the local polarization response in real-space. Nevertheless, this task becomes difficult for such a high frequency. In this sense, the present simulation seems to be unique for bridging the relationship

between the dielectric response in microwave frequency and the strain via the microscopic domain scale.

Methods

Calculation of *ac* dielectric permittivity. The temporal evolution of the dipole lattice is tracked by solving the Ginzburg-Landau (TDGL) equation which takes the following form:

$$\frac{\partial P(r,t)}{\partial t} = -D\frac{\delta F}{\delta P(r,t)}, \tag{10}$$

where t is time scaled in unit τ with $\tau^{-1}=|A_1|D$, and D is the kinetic coefficient. We also calculate the dielectric permittivity as a function of E_{ext}. For a dielectric system that cannot polarize instantaneously in response to an electric field, the total electric polarization as a function of t can be described as:

$$P(t) = \int_{-\infty}^{t} \varepsilon(t-t')E_{ext}(t')dt', \tag{11}$$

where $P(t)$ is a convolution of electric field $E(t)$ at previous times with time-dependent permittivity $\varepsilon(t)=\varepsilon_r(t)+i\varepsilon_i(t)$. Therefore, its Fourier transformation can be directly written as

$$P(\omega) = \varepsilon(\omega)E_{ext}(\omega), \tag{12}$$

where $P(\omega)$ and $E_{ext}(\omega)$ are the Fourier transformations of $P(t)$ and $E_{ext}(t)$ respectively[32]. For the case of *ac* sine electric field such as $E_{ext}(t)=E_0\cdot\sin(\omega_0 t)$ with $\omega_0=2\pi f_0$ and $\omega=2\pi f$, $E_{ext}(\omega)$ can be directly written as:

$$E_{ext}(\omega) = E'_0\delta(\omega-\omega_0), \tag{13}$$

where E'_0 is the coefficient of Fourier transformation and ω_0 is the frequency. Polarization $P(\omega)$ can be calculated by Fourier-transforming the temporal evolution spectrum $P(r, t)$ in Eq.(10). In details, the real-spatial spectrum of $P(r, t)$ at site r and its spatial average $P(t)$ over sufficient number of time periods is calculated by solving Eq.(10). The Fourier-transformed frequency spectrum $P(r, \omega)$ can be expressed as:

$$P(r,\omega) = \int_0^{\infty} P(r,t)e^{-i\omega t}dt, \tag{14}$$

which is used to transform $P(r, t)$ and $P(t)$ into frequency domain to obtain $P(r, \omega)$ and $P(\omega)$. Subsequently, one can compute the corresponding dielectric permittivity $\varepsilon(r, \omega_0)$ at site r and its spatial average $\varepsilon(\omega_0)$ at frequency ω_0 using Eq.(12).

1. Dawber, M., Rabe, K. M. & Scott, J. F. Physics of thin-film ferroelectric oxides. *Rev. Mod. Phys.* **77**, 1083 (2005).
2. Scott, J. F. *Ferroelectric Memories* (Springer, Berlin, 2000).
3. Liu, S. W. *et al.* Ferroelectric (Pb, Sr)TiO_3 epitaxial thin films on (001) MgO for room temperature high-frequency tunable microwave elements. *Appl. Phys. Lett.* **87**, 142905 (2005).
4. Dimos, D. & Mueller, C. H. Perovskite thin films for high-frequency capacitor applications. *Annu. Rev. Mater. Sci.* **28**, 397 (1998).
5. Nelson, C. T. *et al.* Domain dynamics during ferroelectric switching. *Science* **334**, 968 (2011).
6. Ganpule, C. S. *et al.* Polarization relaxation kinetics and 180° domain wall dynamics in ferroelectric thin films. *Phys. Rev. B* **65**, 014101 (2001).
7. Wang, L.-F. & Liu, J.-M. Enhanced piezoelectric effect of relaxor ferroelectrics in nonpolar direction. *Appl. Phys. Lett.* **90**, 062905 (2007).
8. Haeni, J. H. *et al.* Room-temperature ferroelectricity in strained $SrTiO_3$. *Nature* **430**, 758 (2004).
9. Uwe, H. & Sakudo, T. Stress-induced ferroelectricity and soft phonon modes in $SrTiO_3$, *Phys. Rev. B* **13**, 271 (1976).
10. Li, Y. L., Hu, S. Y., Liu, Z. K. & Chen, L. Q. Effect of substrate constraint on the stability and evolution of ferroelectric domain structures in thin films. *Acta. Mater.* **50**, 395 (2002).
11. Liu, Y. Y., Zhu, Z. X., Li, J.-F. & Li, J. Y. Misfit strain modulated phase structures of epitaxial $Pb(Zr_{1-x}Ti_x)O_3$ thin films: The effect of substrate and film thickness. *Mech. Mater.* **42**, 816 (2010).
12. Mueller, V. Dynamics of ferroelectric domain walls. *Adv. Solid State Phys.* **41**, 601 (2001).
13. Eitel, R. E., Shrout, T. R. & Randall, C. A. Nonlinear contributions to the dielectric permittivity and converse piezoelectric coefficient in piezoelectric ceramics. *J. Appl. Phys.* **99**, 124110 (2006).
14. Pramanick, A., Damjanovic, D., Nino, J. C. & Jones, J. L. Subcoercive cyclic electrical loading of lead zirconate titanate ceramics I: nonlinearities and losses in the converse piezoelectric effect. *J. Am. Ceram. Soc.* **92**, 2291 (2009).
15. Griggoio, F. *et al.* Substrate clamping effects on irreversible domain wall dynamics in lead zirconate titanate thin films. *Phys. Rev. Lett.* **108**, 157604 (2012).
16. Rivera-Calzada, A. *et al.* Tailoring interface structure in highly strained YSZ/STO heterostructures. *J., Adv. Mater.* **23**, 5268 (2011).
17. Fousek, J. & Brezina, B. Relaxation of 90° domain walls of $BaTiO_3$ and their equation of motion. *J. Phys. Soc. Jpn.* **19**, 830 (1964).
18. Pertsev, N. A., Arlt, G. & Zembilgotov, Prediction of a giant dielectric anomaly in ultrathin polydomain ferroelectric epitaxial films. A. G., *Phys. Rev. Lett.* **76**, 1364 (1996).
19. Arlt, G., Dederichs, H. & Herbiet, R. 90°-domain wall relaxation in tetragonally distorted ferroelectric ceramics. *Ferroelectrics* **74**, 37 (1987).
20. Wang, J., Shi, S. Q., Chen, L. Q., Li, Y. & Zhang, T. Y. Phase field simulations of ferroelectric/ferroelastic polarization switching. *Acta. Mater.* **52**, 749 (2004).
21. Li, L. J., Yang, Y., Shu, Y. C. & Li, J. Y. Continuum theory and phase-field simulation of magnetoelectric effects in multiferroic bismuth ferrite. *J. Mech. Phys. Solids* **58**, 1613 (2010).
22. Nambu, S. & Sagala, D. A. Domain formation and elastic long-range interaction in ferroelectric perovskites. *Phys. Rev. B* **50**, 5838 (1994).
23. Pertsev, N. A. & Arlt, G. Forced translational vibrations of 90° domain walls and the dielectric dispersion in ferroelectric ceramics. *J. Appl. Phys.* **74**, 4105 (1993).
24. Chen, D. P. & Liu, J.-M. Dynamic hysteresis of tetragonal ferroelectrics: The resonance of 90°-domain switching. *Appl. Phys. Lett.* **100**, 062904 (2012).
25. Li, Y. L., Hu, S. Y., Liu, Z. K. & Chen, L. Q. Effect of substrate constraint on the stability and evolution of ferroelectric domain structures in thin films. *Acta. Mater.* **50**, 395 (2002).
26. Cao, W. & Cross, L. E. Theory of tetragonal twin structures in ferroelectric perovskites with a first-order phase transition. *Phys. Rev. B* **44**, 5 (1991).
27. Potter, Jr, B. G., Tikare, V. & Tuttle, B. A. Monte Carlo simulation of ferroelectric domain structure and applied field response in two dimensions. *J. Appl. Phys.* **87**, 4415 (2000).
28. Hu, H.-L. & Chen, L. Q. Computer simulation of 90° ferroelectric domain formation in two-dimensions. *Mater. Sci. Eng. A.* **238**, 182 (1997).
29. Liu, J.-M., Wang, X., Chan, H. L. W. & Choy, C. L. Monte Carlo simulation of the dielectric susceptibility of Ginzburg-Landau mode relaxors. *Phys. Rev. B* **69**, 094114 (2004).
30. Li, B. L., Liu, X. P., Fang, F. & Liu, J.-M. Monte Carlo simulation of ferroelectric domain growth. *Phys. Rev. B* **73**, 014107 (2006).
31. Wang, L. F. & Liu, J.-M. Role of long-range elastic energy in relaxor ferroelectrics. *Appl. Phys. Lett.* **89**, 092909 (2006).
32. Chu, P., Chen, D. P. & Liu, J.-M. Multiferroic domain structure in orthorhombic multiferroics of cycloidal spin order: Phase field simulations. *Appl. Phys. Lett.* **101**, 042908 (2012).
33. Hu, H. L. & Chen, L. Q. Three-dimensional computer simulation of ferroelectric domain formation. *J. Am. Ceram. Soc.* **81**, 492 (1998).
34. Mitsui, T., Tatsuzaki, I. & Nakamura, E. *An introduction to the physics of ferroelectrics* (Gordon and Breach, New York, 1976).
35. Buixaderas, E. *et al.* Lattice dynamics and dielectric response of undoped, soft and hard $PbZr_{0.42}Ti_{0.58}O_3$. *Phase Transitions* **83**, 917 (2010).
36. Kersten, J. & Schmidt, G. Dielectric dispersion in PZT ceramics. *Ferroelectrics* **67**,191 (1986).
37. Pertsev, N. A. & Arlt, G. Forced translational vibrations of 90° domain walls and the dielectric dispersion in ferroelectric ceramics. *J. Appl. Phys.* **74**, 4415 (1993).
38. Alldredge, L. M. B., Chang, W., Kirchoefer, S. W. & Pond, J. M. Microwave dielectric properties of $BaTiO_3$ and $Ba_{0.5}Sr_{0.5}TiO_3$ thin films on (001) MgO. *Appl. Phys. Lett.* **95**, 222902 (2009).
39. Fardin, E. A. *et al.* Polycrystalline $Ba_{0.6}Sr_{0.4}TiO_3$ thin films on r-plane sapphire: Effect of film thickness on strain and dielectric properties. *Appl. Phys. Lett.* **89**, 182907 (2006).

Acknowledgements:

This work was supported by the National 973 Projects of China (Grants No. 2011CB922101), the Natural Science Foundation of China (Grants Nos. 11234005, 11374147, and 51332006), and the Priority Academic Program Development of Jiangsu Higher Education Institutions, China. Li also acknowledges the support of NSF (CMMI-1100339).

Author contributions

J.M.L. conceived the research project and P.C. performed the computations. D.P.C., Y.L.W., Y.L.X., Z.B.Y., J.G.W. and J.Y.L. commented the modeling and discussed the results. P.C. and J.M.L. wrote the paper.

Additional information

Supplementary information accompanies this paper at http://www.nature.com/scientificreports

Competing financial interests: The authors declare no competing financial interests.

How to cite this article: Chu, P. *et al.* Kinetics of 90° domain wall motions and high frequency mesoscopic dielectric response in strained ferroelectrics: A phase-field simulation. *Sci. Rep.* **4**, 5007; DOI:10.1038/srep05007 (2014).